



First-principles study on surface structure, thickness and composition dependence of the stability of Pt-skin/Pt₃Co oxygen-reduction-reaction catalysts

Mary Clare Sison Escaño^{a,*}, Hideaki Kasai^b

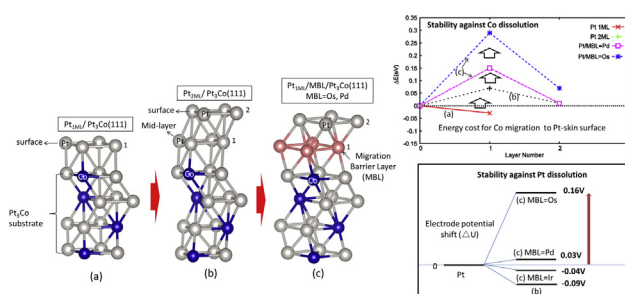
^a Graduate School of Engineering, University of Fukui, 3-9-1 Bunkyo, Fukui 910-8507, Japan

^b Department of Applied Physics, Osaka University, 2-1 Yamada-oka, Suita 565-0871, Japan

HIGHLIGHTS

- Thicker Pt-skin is more stable against Co dissolution under oxygen environment.
- The O_{ad} site differentiates stability between (111) and (100) Pt-skin structures.
- Thicker Pt-skin is as stable as pure Pt catalyst against Pt dissolution.
- Low-cost and stable MBL (Os,Pd)-substituted Pt-skin ORR catalysts are introduced.

GRAPHICAL ABSTRACT



ARTICLE INFO

Article history:

Received 16 July 2013

Received in revised form

22 August 2013

Accepted 3 September 2013

Available online 12 September 2013

Keywords:

Pt-skin

ORR catalysts

Pt–Co alloys

PEMFC

Stability

Density functional theory

ABSTRACT

The stability of Pt-skin on Pt₃Co alloy against Co and Pt dissolution with respect to Pt-skin thickness, surface structure and composition is investigated using density functional theory calculations. It is found that, even under oxygen environment, Co migration to the surface is suppressed by the thicker Pt-skin (2–3 Pt atomic layers), confirming experiments. However, the instability of single Pt layer is attributed to the electronic effect of oxygen. The adsorbed oxygen redistributes charge from Pt–Co region to Pt–O region, weakening the Pt–Co bond and facilitating Co migration to surface via Co–O bond formation. We further note that in this system, the Co migrates easier in (111) surface than in (100), attributed to the difference in the oxygen adsorption sites (fcc vs bridge). A minimal negative electrode potential shift of 0.06–0.09 V for Pt dissolution is noted for thicker Pt-skin systems, indicating stability close to pure Pt. The Pt-skin composition is varied by introducing different Migration Barrier Layers (MBLs) = Ru, Rh, Pd, Os, Ir, in the mid-Pt-skin region and found that when MBL is Os or Pd, a novel low-cost composition and more stable MBL-substituted Pt-skin/Pt₃Co ORR catalyst emerges.

© 2013 Elsevier B.V. All rights reserved.

1. Introduction

Overall, the cost, performance and durability of the catalyst are the three most important factors that affect commercialization of polymer membrane electrolyte fuel cell (PEMFC). It is well-known

* Corresponding author.

E-mail address: mcescano@u-fukui.ac.jp (M.C.S. Escaño).

that the kinetics of the oxygen-reduction-reaction (ORR) at the cathode is still sluggish even on Pt. At present, the most promising near-term electrocatalyst for the ORR are seen to be Pt-based alloy systems [1–4]. Among these, the Pt–Co systems have received a considerable attention because of high ORR activity [2,4] and better stability in acidic environment [5–7]. Thus, further nanostructuring of Pt–Co systems for an enhanced performance and stability as compared to the conventional pure Pt catalysts, while maintaining a low Pt loading, is of tremendous interest. However, the loss of the

3d transition metals through easy formation of surface oxides is known to significantly reduce the ORR activity in Pt alloys after some potential cycling, and therefore limits the use of these systems in PEMFC [1–4]. It has been observed experimentally that a typical pure Pt outerlayer, often called “Pt-skin”, is formed on Pt–Co systems after electrochemical stabilization of the As-prepared alloy or under electrochemical measurements [1,4,8,9]. Such Pt layer formation on the alloy surface was also found in other Pt–3d transition metal combinations [3,4,10,11]. Despite the fact that the Pt-skin (“outerlayer” and “skin” are used interchangeably) can serve as a protective covering, Co dissolution is not significantly eliminated [8]. It was shown by STM image that the Pt outerlayer has (111) surface structure [8]. However, more recent experiment, involving the same (111) surface, but with a thicker Pt-skin (i.e. 2 Pt layers) formed by nanocapsule method, reports better stability against Co dissolution [12]. Next, another experiment reports superior stability against Co dissolution upon potential cycling for annealed nanoparticles of 5–7 nm sizes. These systems exhibit a (100) surface structure of the Pt-skin and is composed of 2–3 atomic Pt layers [13]. Moreover, the loss of electrochemical active surface area (ECSA) is found to be minimal even after 5000 cycles. These experimental researches have motivated the present study to explore the atomic level properties and energetics of Co dissolution with respect to the: (1) Pt-skin thickness and (2) surface structure, which has not been explored. A first-principles study based on density functional theory (DFT) is conducted on the migration behavior of Co from the alloy substrate to the surface of the Pt-skin, accompanied by Co–O bond formation on surface. Based on the experiments on Pt–Co systems [8,12,13], alloy surfaces are often found to be decorated by Co oxides, which eventually dissolve into the acid solution. Theoretical works have explored the dissolution of 3d transition metals, mostly Co, Ni and Fe, in Pt–3d alloys as well as in the Pt monolayer on Pt–3d alloys [14–16]. These studies have reported ease of 3d transition metal migration with O coverage as compared to that of the zero coverage. More recently, the oxygen adsorbate-induced segregation of Co has been reported for Pt–Co alloy at nanoscale [17]. Since the mechanism for this observation is also lacking, it is therefore necessary to seek the origin of the influence of oxygen in the dissolution, in particular, the Co, within an electronic perspective. For completeness of stability evaluation, the electrochemical potential shift of Pt dissolution in the thicker Pt skin systems and of different surface structure is further evaluated and compared with the pure Pt catalysts. Lastly, a quest for new design of Pt-skin has prompted this research to undertake a non-Pt mid-layer substitution in the thicker Pt-skin systems. The mid-layer (herein termed as Migration Barrier Layer or MBL) is composed of either one of the following metals: Ru, Rh, Pd, Os, Ir. Basically, these 4d and 5d-transition metals have been considered in magnetic multilayers in spintronics as “capping” layers to prevent oxidation or intermixing of metals [18–20]. Here, the reactivity and stability against Co and Pt dissolution of the MBL-substituted Pt-skin catalysts under oxygen environment are evaluated. This screening of MBLs could give way for a viable Pt-skin composition on Pt₃Co alloy. It is viewed that this present study provides new insights into the migration of Co to the surface with respect to different Pt-skin structures, thickness and composition, thereby aid in furthering the design of stable Pt-skin/Pt₃Co ORR catalyst for PEMFC cathode. Also, a novel and potentially more stable and more reactive Pt-skin composition on Pt–Co alloy is drawn.

2. Computational methods

The first-principles study is conducted within the spin-polarized density functional theory (DFT) [21,22] framework using Projector Augmented Wave (PAW) method [23] and plane-wave

basis set. The calculations are performed using the spin-polarized version of Vienna *ab initio* Simulation Package (VASP) [24–27] which can properly treat magnetic character of O₂ and Co. The Pt–Co alloy surface is modeled using L₁₂-ordered Pt₃Co bulk structure cut in (111) and (100) directions. The L₁₂ structure of the bulk alloy is composed of Pt atoms at the face centers and the Co atoms at the corners of the cell. Therefore two slabs have been formed: Pt₃Co(111) and Pt₃Co(100). The Pt-skin on Pt–Co systems are modeled by laying 1, 2, or 3 atomic layers of Pt pseudo-morphically on Pt₃Co(111) and Pt₃Co(100) slabs. This enables attainment of the same surface structure as the slab. The multiple layers of the Pt-skin also attain a fcc stacking. The surface unit cell size is (2 × 2) and the vacuum size is ~12.0 Å. The optimized surfaces are obtained by relaxing the Pt layers and the two top-most layers of the Pt₃Co substrates. The optimized structures are shown in Figs. 1 and 2 (for side views only, the corresponding top views are given in Figs. 5 and 7) and are denoted as either Pt_nML/Pt₃Co(111) and Pt_nML/Pt₃Co(100) (depending on the facet of the Pt₃Co substrate), where *n* is the number of Pt atomic layers composing the Pt-skin. Details of the atomic structure and stability evaluation are discussed in the next section. At this point however, it worthwhile to mention that the model systems {Pt_nML/Pt₃Co(111) and Pt_nML/Pt₃Co(100)} appropriately describe the multiple Pt-skin layers, the resulting surface structures and the uniform Pt₃Co substrate/core composition observed in experiments [12,13] as previously discussed in the introduction. Next, A plane-wave expansion with a cutoff energy of 400 eV is used throughout the calculations. The conjugate-gradient method [28] is used for the relaxations and the positions of the atoms are moved until the maximum force (on each atom) is converged to less than 0.02 eV Å^{−1}. The generalized gradient approximation (GGA) based on the Perdew, Burke and Ernzerhof (PBE) functional [29] is used for the exchange–correlation correction. Brillouin-zone integrations are performed on a grid of (4 × 4 × 1) Monkhorst-Pack *k* points with a smearing of Methfessel–Paxton method [30]. These calculation parameters are tested and rendered an excellent agreement of equilibrium lattice parameters of fcc-Pt, fcc-Co and L₁₂-Pt₃Co {Pt: 3.97 Å, Co: 3.52 Å, Pt₃Co: 3.89 Å} with experiments {Pt: 3.96 Å [31], Co 3.55 Å [32], Pt₃Co: 3.85 Å [33]}. For the oxygen, the DFT-GGA implementation yields a bond length of 1.24 Å and a dissociation energy of 5.67 eV, in general agreement with experiment (1.21 Å; 5.25 eV) [34] and with other DFT–GGA calculations (1.24 Å; 5.64 eV) [35,36].

3. Results and discussions

3.1. Atomic structures of Pt_nML/Pt₃Co systems

As discussed previously, the Pt-skin on Pt–Co alloys are represented by Pt_nML/Pt₃Co systems, where *n* = 1, 2, or 3 Pt atomic layers. Thus a total of six Pt_nML/Pt₃Co structures are considered in this study – three structures belonging to each of (111) and (100) facets. The systems are denoted as: Pt₁ML/Pt₃Co(111), Pt₂ML/Pt₃Co(111), and Pt₃ML/Pt₃Co(111) for the (111) facet as shown in Fig. 1(a)–(c) and Pt₁ML/Pt₃Co(100), Pt₂ML/Pt₃Co(100), and Pt₃ML/Pt₃Co(100) for (100) facet as shown in Fig. 2(a)–(c). The pure Pt outerlayers are labeled as 1, 2 and 3 beginning from the top of the Pt₃Co substrate. Regarding the Pt₃Co(111) substrate, each layer is composed of 3 Pt atoms and 1 Co atom as shown in Fig. 1. The relevant bond lengths and interlayer distances are given from the 2nd to the 5th column of Table 1. The first interlayer distance (*d*_{0–1}) are generally larger than that of pure Pt(111). The rest of the interlayer distances (*d*_{1–2}, *d*_{2–3}) show a quite wider range of values across different Pt-skin thickness. However, Pt–Co bond length (*d*_{Pt–Co}), remains unchanged with respect to the Pt-skin thickness. The lateral Pt–Pt

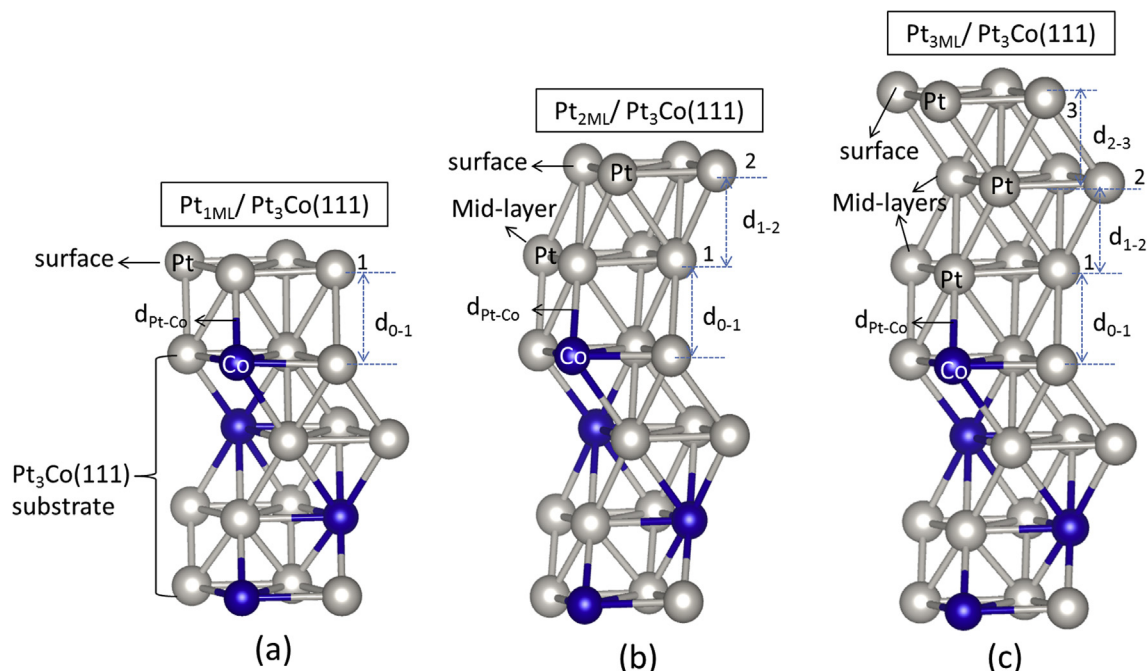


Fig. 1. Optimized atomic structure of $\text{Pt}_{n\text{ML}}/\text{Pt}_3\text{Co}(111)$. (a), (b) and (c) correspond to $n = 1$, $n = 2$ and $n = 3$, respectively. The $\text{Pt}_3\text{Co}(111)$ substrate is indicated in (a). The interlayer distances, d_{0-1} , d_{1-2} and d_{2-3} , the Pt surface, Pt mid-layers and the $d_{\text{Pt-Co}}$ bond are shown.

distance in the alloy system (2.75 \AA) is shorter than that of the pure Pt (2.81 \AA). In the case of the $\text{Pt}_{n\text{ML}}/\text{Pt}_3\text{Co}(100)$ structures [Fig. 2(a)–(c)], almost the same trend in the interlayer distances can be observed (7th to the 11th column of Table 1). The d_{0-1} is also larger than that of pure Pt(100) and there is also wide range of values for

the upper interlayers (d_{1-2} , d_{2-3}). However, contrary to $\text{Pt}_{n\text{ML}}/\text{Pt}_3\text{Co}(111)$, the $d_{\text{Pt-Co}}$ varies with the thickness of the Pt-skin. The $d_{\text{Pt-Co}}$ is larger for thicker Pt-skin. The lateral Pt–Pt distance is the same as that in pure Pt(100), 2.81 \AA . It should be noted that the $\text{Pt}_3\text{Co}(100)$ substrate is obtained by interchanging the Co and Pt

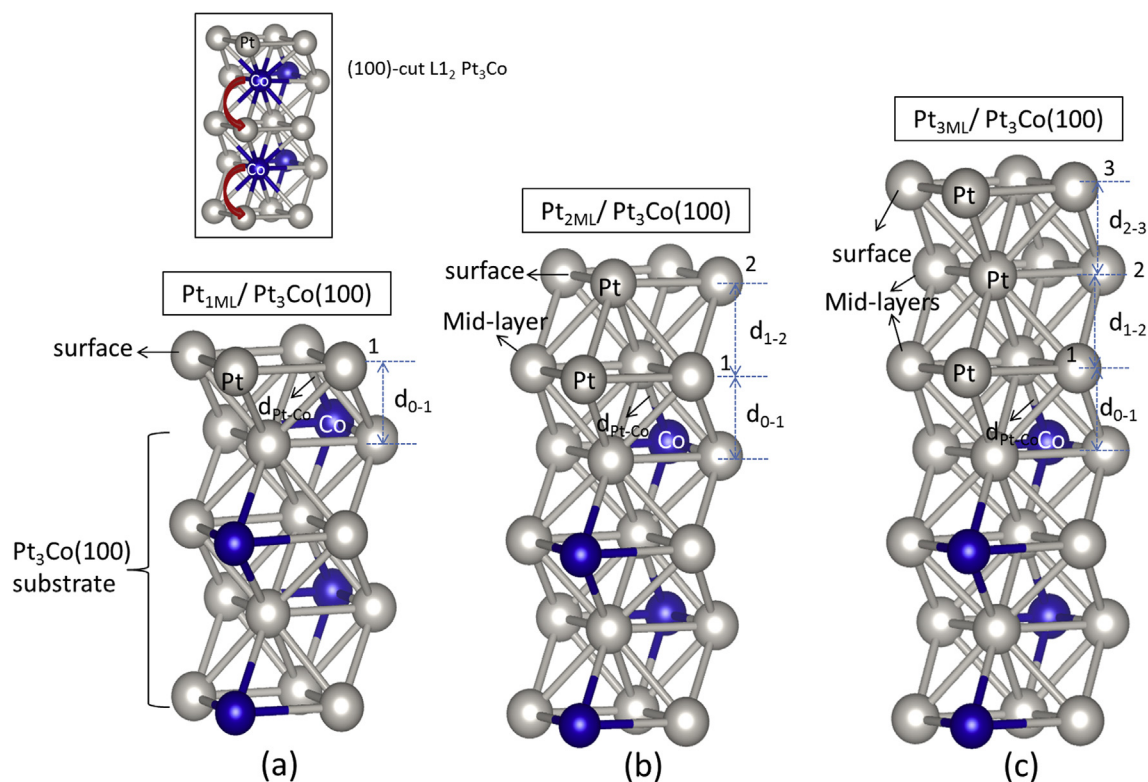


Fig. 2. Optimized geometry of $\text{Pt}_{n\text{ML}}/\text{Pt}_3\text{Co}(100)$. (a), (b) and (c) correspond to $n = 1$, $n = 2$ and $n = 3$, respectively. The $\text{Pt}_3\text{Co}(100)$ substrate is labeled in (a). The interlayer distances, d_{0-1} , d_{1-2} and d_{2-3} , the Pt surface, Pt mid-layers and the $d_{\text{Pt-Co}}$ bond are shown. The inset figure shows the (100)-cut $\text{L1}_2\text{-Pt}_3\text{Co}$ with Co shift in position to attain consistency of Co composition per layer as that used in $\text{Pt}_3\text{Co}(111)$ substrate.

Table 1

Atomic structure (i.e. interlayer distances (d_{0-1} , d_{1-2} , d_{2-3}), Pt–Co bond length ($d_{\text{Pt-Co}}$) and lateral Pt–Pt distances) of the $\text{Pt}_{n\text{ML}}/\text{Pt}_3\text{Co}(111)$, $\text{Pt}_{n\text{ML}}/\text{Pt}_3\text{Co}(100)$, $\text{Pt}(111)$ and $\text{Pt}(100)$. Experimental d_{0-1} for pure $\text{Pt}(111)$ and $\text{Pt}(100)$ are given in parenthesis.

	$\text{Pt}_{n\text{ML}}/\text{Pt}_3\text{Co}(111)$ (Å)					$\text{Pt}_{n\text{ML}}/\text{Pt}_3\text{Co}(100)$ (Å)				
	d_{0-1}	d_{1-2}	d_{2-3}	$d_{\text{Pt-Co}}$	Pt–Pt	d_{0-1}	d_{1-2}	d_{2-3}	$d_{\text{Pt-Co}}$	Pt–Pt
Pt 1 ML	2.31	—	—	2.72	2.75	1.90	—	—	2.73	2.81
Pt 2 ML	2.39	2.28	—	2.72	2.75	1.97	1.94	—	2.78	2.81
Pt 3 ML	2.39	2.38	2.30	2.72	2.75	1.96	1.96	1.96	2.78	2.81
Pure Pt	2.31 (2.26) ³¹				2.81	1.93 (1.94) ⁴⁸				2.81

atom underneath (see inset figure). The actual (100)-cut $\text{L}_{12}\text{-Pt}_3\text{Co}$ structure has originally two Co atoms in an “alternating” Pt_3Co substrate’s layers. However, for consistency with the composition of Co atoms with the $\text{Pt}_3\text{Co}(111)$, then one Co atom should be moved to the next lower substrate layer as shown by the arrows. Although this leads to a system with quite a higher energy, it allows for a suitable and reliable comparison of Co migration as a function of Pt surface structure and thickness.

Next, the energetics of the migration of Co to the surface for the bare $\text{Pt}_{n\text{ML}}/\text{Pt}_3\text{Co}$ for both (111) and (100) facets is obtained by interchanging the Pt (in higher layer) with the Co (in the lower layer) and then calculating the energy change (ΔE) upon this Co upshift (i.e. migration). This scheme is shown in the Fig. 3 (inset). For all systems, the reference energy for ΔE is the total energy of the initially optimized Pt-skin structures as depicted in Figs. 1 and 2. The ΔE is calculated for all values of n . For the $\text{Pt}_{n\text{ML}}/\text{Pt}_3\text{Co}(111)$, the ΔE plots for Co migration to the surface is shown in Fig. 3 and that for $\text{Pt}_{n\text{ML}}/\text{Pt}_3\text{Co}(100)$ is given in Fig. 4. First, for the $\text{Pt}_{n\text{ML}}/\text{Pt}_3\text{Co}(111)$, it can be noted that there is a very little positive change (endothermic) in migration energy ($\Delta E = 0.02\text{--}0.06$ eV) when Co moves *within* the Pt-skin (indicated as Pt mid-layers in the figure), while there is a large positive change (endothermic) in energy ($\Delta E = 0.65\text{--}0.70$ eV) when Co migrates *from the subsurface to the Pt-skin surface*. In general, this agrees with the theoretical study on segregation of metals, which reports that Pt, and not Co, segregate easily to the surface in a Pt–Co bimetallic system [37]. For the bare $\text{Pt}_{n\text{ML}}/\text{Pt}_3\text{Co}(100)$, the same trend in Co migration to surface can be observed. The ΔE plot is shown in Fig. 4. We note that the ΔE for Co migration in the Pt mid-layers are also minimal, however, we see that there are energies that are downhill (exothermic). This is due

to the fact that the $\text{Pt}_3\text{Co}(100)$ system is formed from interchanging Co and Pt positions to allow for the same composition of Co and Pt per layer as that of $\text{Pt}_3\text{Co}(111)$ system, as discussed previously. Thus, when the Co reached the so called “alternate” layers where they are more stable, a negative change in migration energy can be expected. As in $\text{Pt}_{n\text{ML}}/\text{Pt}_3\text{Co}(111)$, the migration from the subsurface to the Pt surface for all three $\text{Pt}_{n\text{ML}}/\text{Pt}_3\text{Co}(100)$ systems also entail large energy cost ($\Delta E = 0.53\text{--}0.72$ eV). Thus, for both (111) and (100) Pt-skin structures, two generalizations can be deduced: (1) a minimal change in energy is needed to move *within* the Pt-skin and (2) large positive energies are required for Co migration *from subsurface to the surface*.

3.2. Effect of oxygen on Co migration

Because of the suspected role of oxygen in the segregation of Co to the surface via formation of surface oxide, the adsorption of oxygen on all the 6 Pt-skin structures is conducted. The possible adsorption sites of O in $\text{Pt}_{n\text{ML}}/\text{Pt}_3\text{Co}(111)$ is shown in Fig. 5. Bridge (b), hollow (fcc, hcp) and top (t) sites are the main symmetric sites and are further split into various other sites based on the subsurface atoms. Overall, five types of bridge sites are identified, two for hcp, two for fcc and also two for top sites. The adsorption on a (2×2) surface unit cell leads to a 0.25 ML oxygen coverage. The binding energies are calculated based on the following:

$$E_{\text{ads}} = E_T - (E_{\text{slab}} + E_{\text{O atom}})$$

where E_T is the total energy of the adsorbed system, E_{slab} and $E_{\text{O atom}}$ represent the total energies of isolated slab and oxygen

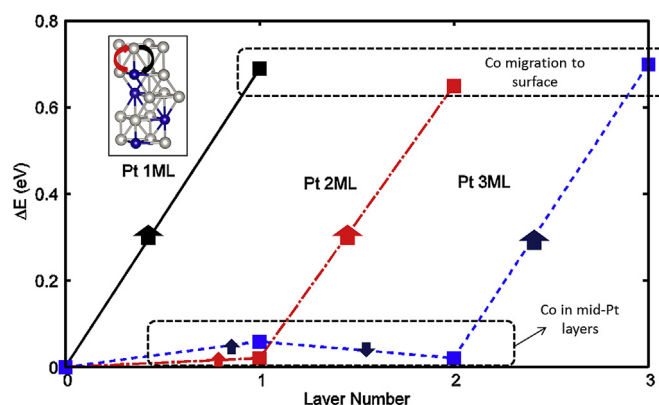


Fig. 3. Co migration energy (ΔE in $\text{Pt}_{n\text{ML}}/\text{Pt}_3\text{Co}(111)$ systems). Up arrows indicate positive ΔE (endothermic) and down arrows depict negative ΔE (exothermic). Sample Pt and Co exchange of positions is illustrated in the inset figure. ΔE is obtained from the total energy of the new Co-migrated $\text{Pt}_{n\text{ML}}/\text{Pt}_3\text{Co}(111)$ system referenced to the initial $\text{Pt}_{n\text{ML}}/\text{Pt}_3\text{Co}(111)$. Regions in the plot where energies corresponding to Co migration to the Pt-skin surface and to that within the Pt mid-layers are shown in dashed boxes.

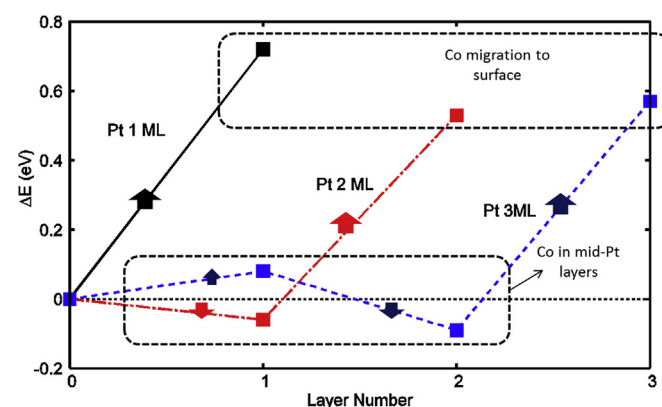


Fig. 4. Co migration energy (ΔE in $\text{Pt}_{n\text{ML}}/\text{Pt}_3\text{Co}(100)$ systems). Up arrows indicate positive ΔE (endothermic) and down arrows depict negative ΔE (exothermic). ΔE is obtained from the total energy of the new Co-migrated $\text{Pt}_{n\text{ML}}/\text{Pt}_3\text{Co}(100)$ system referenced to the initial optimized slab. The same scheme of Co migration towards the surface as that of (111) is used. Regions in the plot where energies corresponding to Co migration to the Pt-skin surface and to that within the Pt mid-layers are shown in dashed boxes.

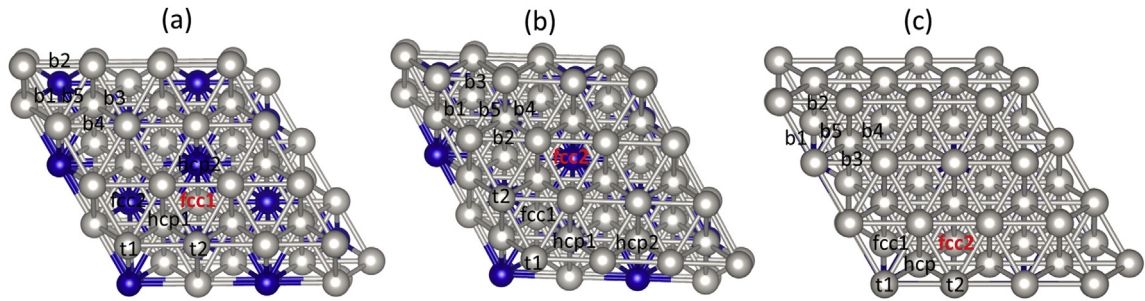


Fig. 5. (a), (b) and (c) show the top views of Pt_{1ML}/Pt₃Co(111), Pt_{2ML}/Pt₃Co(111) and Pt_{3ML}/Pt₃Co(111), respectively. The oxygen atom adsorption sites are labeled accordingly. The most stable site is indicated in bold form.

atom, respectively. Binding energies are given in Table 2. The most stable oxygen adsorption sites are indicated in bold form. It can be noted that the O atom prefers the fcc sites, which is the same as the most favorable adsorption position of oxygen atom in the pure Pt(111). However, the binding energies are lower on the Pt-skin than on the pure Pt and the E_{ads} tends to increase upon increase of the thickness of the Pt-skin. The lower binding energy of O atom on other Pt-3d transition metal alloy systems as compared to that of pure Pt has also been reported [38–41]. We further note that the

Table 2
Adsorption sites and corresponding binding energies (E_{ads}) of oxygen atom on Pt_{nML}/Pt₃Co(111), Pt_{nML}/Pt₃Co(100), Pt(111) and Pt(100). The most stable adsorption sites are indicated in bold form. The bridge sites for (111) facet relaxes to the nearby fcc sites and the final state is indicated in the superscript. b* for pure Pt(111) indicates the local minima is found using residual minimization (RMM-DIIS) algorithm.

Pt _{nML} /Pt ₃ Co(111)			Pt _{nML} /Pt ₃ Co(100)		
	Site	E_{ads} (eV)		Site	E_{ads} (eV)
Pt 1 ML	t1	−3.76	Pt 2 ML	t1	−3.44
	t2	−2.90		t2	−3.51
	hcp1	−3.72		h1	−4.27
	hcp2	−3.76		h2	−4.14
	fcc1	−4.12		b1	−4.34
	fcc2	−3.85		b2	−4.32
	b1	−3.85 ^{fcc2}			
	b2	−3.85 ^{fcc1}			
	b3	−4.12 ^{fcc1}			
	b4	−4.12 ^{fcc1}			
Pt 2 ML	b5	−3.85 ^{fcc2}			
	t1	−2.96		t1	−3.47
	t2	−2.91		t2	−3.48
	hcp1	−3.87		h1	−4.15
	hcp2	−3.89		h2	−4.21
	fcc1	−4.22		b1	−4.48
	fcc2	−4.30		b2	−4.46
	b1	−4.22 ^{fcc1}			
	b2	−4.22 ^{fcc1}			
	b3	−4.22 ^{fcc1}			
Pt 3 ML	b4	−4.22 ^{fcc1}			
	b5	−4.22 ^{fcc1}			
	t1	−2.95		t	−3.55
	t2	−2.98		h	−4.23
	hcp	−3.92		b	−4.60
	fcc1	−4.28			
	fcc2	−4.32			
	b1	−4.28 ^{fcc1}			
	b2	−4.28 ^{fcc1}			
	b3	−4.28 ^{fcc1}			
Pure Pt	b4	−4.32 ^{fcc2}			
	b5	−4.28 ^{fcc1}			
	t	−3.06			
	hcp	−4.01			
	fcc	−4.46			
	b	−4.46 ^{fcc}			
	b*	−3.74 ^(RMM)			

bridge sites are not the global minima since the oxygen slides to adjacent fcc-sites as indicated in Table 2. This is due to the conjugate gradient algorithm used in the optimization as mentioned in the computational method section. This method searches for the global minimum and not the local minima. This is verified by the test on pure Pt(111) using residual minimization method (RMM-DIIS) [42,43], known for the local minima identification. The binding energy for bridge site (b* in Table 2) is obtained. The location of bridge site in Pt(111) using this algorithm is in agreement with previous work [44]. Next, the slight destabilization of O atom on catalyst surface as compared to the conventional Pt catalyst is often taken as a predictor of better ORR activity. The less bound O adsorbates can facilitate protonation leading to easier formation of intermediate species in the over-all ORR reaction pathways [45,46]. Under 0.25 ML oxygen coverage, the migration energy profile for Co in Pt_{nML}/Pt₃Co(111) is now changed. In Fig. 6(a), it is shown that the Co migration in single Pt layer on Pt₃Co(111) to the surface is exothermic, $\Delta E = -0.03$ eV (while endothermic in zero-coverage). The Co–O bond formation on the surface is shown in the inset figure. For the thicker Pt-skins {Pt₂–Pt_{3ML}/Pt₃Co(111)}, the ΔE are all positive. However, the migration from Pt subsurface to the surface is downhill, that is, when compared to the previous step (see the down arrows at the end for $n = 2$ and $n = 3$). It is also worthwhile to note that when the migration of Co in the zero oxygen coverage (Fig. 3) and in the 0.25 ML coverage (Fig. 6) are compared, the trends in the movement of Co within the Pt-skin is preserved (same sequence of up and down arrows). In fact, the positive ΔE for the migration in the middle

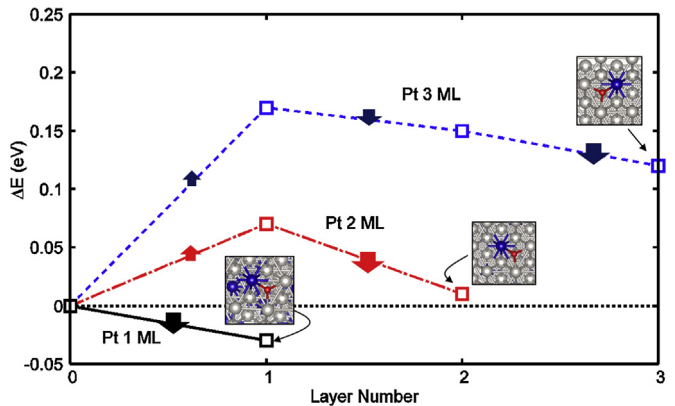


Fig. 6. Co migration energy (ΔE in Pt_{nML}/Pt₃Co(111) systems under 0.25 ML oxygen coverage. Up arrows indicate positive ΔE (endothermic) and down arrows depict negative ΔE (exothermic). The same scheme of Co migration towards the surface as that of bare Pt_{nML}/Pt₃Co(111) slab is used. The Co–O bond formation on the surface is shown in the inset figures, corresponding to the Co migration from subsurface to the surface (indicated by line arrows).

layers are greater in $\text{Pt}_{2-3\text{ML}}/\text{Pt}_3(\text{Co}111)$ under 0.25 ML oxygen coverage than in the zero oxygen coverage. Thus, two important characteristics of Co migration with varied Pt-skin thickness under oxygen coverage can be derived. First, the thicker Pt layers can stabilize Co within the system, which now confirms the experimental observation on stable $\text{Pt}_{\text{skin}}/\text{Pt}_3\text{Co}$ with 2–3 Pt atomic layers against Co dissolution [12,13]. Secondly, the Co migration becomes downhill in energy only when the subsurface (one layer below the surface) is reached. This explains the experimental observation that Co dissolution is mostly prevalent in a 1 atom layer-thick Pt skin over Pt–Co alloy [4,8].

Similarly, the adsorption of O atom is investigated for $\text{Pt}_{n\text{ML}}/\text{Pt}_3\text{Co}(100)$. The adsorption sites are shown in Fig. 7. The hollow (h), bridge (b) and top (t) sites are also further split into two differing oxygen positions (e.g. b1 and b2 for bridge site, and so on). The binding energies are also provided in Table 2. The most stable site is labeled in bold form. In the same way, the E_{ads} in the $\text{Pt}_{n\text{ML}}/\text{Pt}_3\text{Co}(100)$ are lower than that of the pure Pt(100). The most stable bridge site adsorption in Pt(100) is also preserved in the Pt-skin systems. Fig. 8 shows the change in the migration energy, ΔE of Co for different Pt overlayer thickness. For $\text{Pt}_{1\text{ML}}/\text{Pt}_3\text{Co}(100)$, the migration is surprisingly endothermic with a small positive energy, $\Delta E = 0.04$ eV. In fact, the Co migration from the subsurface to the Pt-skin surface for all thickness is endothermic (shown by the up arrows at the end for $n = 2$ and $n = 3$). This is something to be looked into especially when compared to the exothermic migration of Co from Pt subsurface to surface in (111) facet (down arrows at the end for $n = 2$ and $n = 3$ as shown previously in Fig. 6). The mechanism of this difference in the Co migration with respect to facet is discussed later. Next, the same combination of exothermic and endothermic Co migration within the Pt mid-layers for thicker $\text{Pt}_{2-3\text{ML}}/\text{Pt}_3\text{Co}(100)$ systems as that with their bare slabs (Fig. 4) is observed. Thus, for thicker $\text{Pt}_{2-3\text{ML}}/\text{Pt}_3\text{Co}(100)$ systems, the oxygen also does not affect the movement of Co within the Pt-skin, similar to that of $\text{Pt}_{n\text{ML}}/\text{Pt}_3\text{Co}(111)$. In addition to the presence of positive ΔE , the above results can explain the experimentally observed stability of Pt overlayer with (100) structure against potential cycling [13].

3.3. Mechanism of the effect of oxygen

The striking difference in the energetics of Co migration from subsurface to Pt-skin surface upon O adsorption between (111) and (100) surface structures necessitates a mechanism. In this work, charge density difference is employed before and after O adsorption for $\text{Pt}_{1\text{ML}}/\text{Pt}_3\text{Co}(111)$ and $\text{Pt}_{1\text{ML}}/\text{Pt}_3\text{Co}(100)$ systems to determine the extent of electronic effect caused by oxygen via a

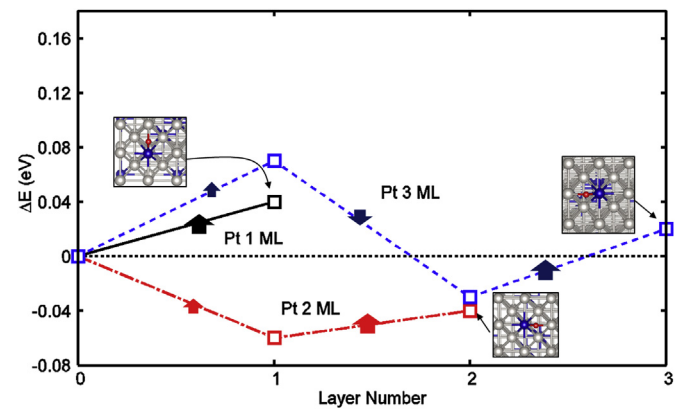


Fig. 8. Co migration energy (ΔE in $\text{Pt}_{n\text{ML}}/\text{Pt}_3\text{Co}(100)$ systems under 0.25 ML oxygen coverage. Up arrows indicate positive ΔE (endothermic) and down arrows depict negative ΔE (exothermic). The same scheme of Co migration towards the surface as that of bare $\text{Pt}_{n\text{ML}}/\text{Pt}_3\text{Co}(100)$ slab is used. The Co–O bond formation on the surface is shown by the inset figures, which correspond to Co migration from subsurface to the surface (indicated by line arrows).

visualization of charge flow. The charge difference is obtained using the following expressions:

$$\rho_T - (\rho_O + \rho_{\text{Pt-skin}})$$

where ρ_T , ρ_O , $\rho_{\text{Pt-skin}}$ are the charge densities of the O-adsorbed $\text{Pt}_{n\text{ML}}/\text{Pt}_3\text{Co}$ systems, isolated O atom and the bare $\text{Pt}_{n\text{ML}}/\text{Pt}_3\text{Co}$ systems, respectively. Similarly, for the bare $\text{Pt}_{n\text{ML}}/\text{Pt}_3\text{Co}$ systems, the charge difference at the first interlayer is obtained via the following:

$$\rho_T - (\rho_{\text{Pt}} + \rho_A)$$

where ρ_T , ρ_{Pt} , ρ_A are the charge densities of the bare $\text{Pt}_{n\text{ML}}/\text{Pt}_3\text{Co}$ systems, isolated Pt layer and the Pt_3Co alloy slab, respectively. Figs. 9 and 10 show the charge redistribution plots for both systems. First, it can be noted that without oxygen coverage {Figs. 9(a) and 10 (a)}, the charge accumulates (dark/red) within the Pt–Co bonds, while, charge is depleted (light/green) in the Pt sites. This supports a strong Pt–Co bonding in the bare systems, which in turn can account for the large positive ΔE . However, when oxygen is adsorbed {Figs. 9(b) and 10(b)}, we note that first, for the O on the fcc site of $\text{Pt}_{1\text{ML}}/\text{Pt}_3\text{Co}(111)$, the charge distribution is reversed. The accumulation of charge is now observed in Pt–O region, while charges are depleted in Pt–Co region {Fig. 9(b)}. The strong Pt–Co bonding noted in the bare system is lost under 0.25 ML oxygen

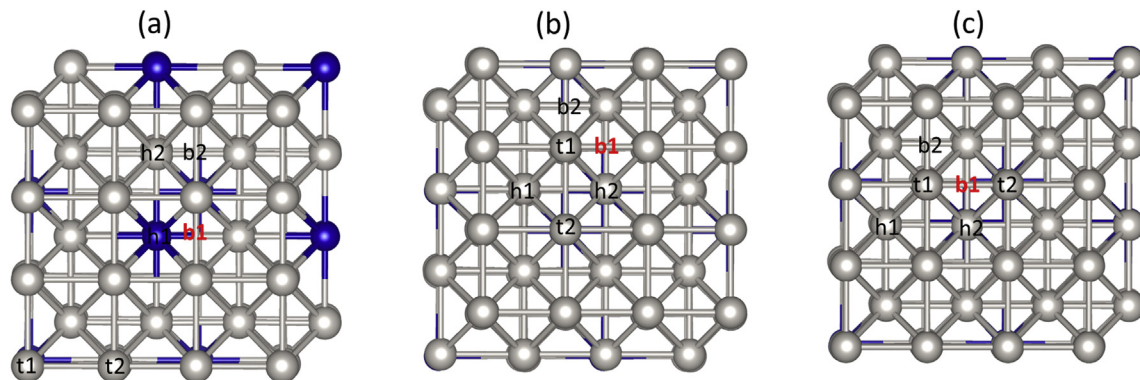


Fig. 7. (a), (b) and (c) show the top views of $\text{Pt}_{1\text{ML}}/\text{Pt}_3\text{Co}(100)$, $\text{Pt}_{2\text{ML}}/\text{Pt}_3\text{Co}(100)$ and $\text{Pt}_{3\text{ML}}/\text{Pt}_3\text{Co}(100)$, respectively. The oxygen atom adsorption sites are labeled accordingly. The most stable site is indicated in bold form.

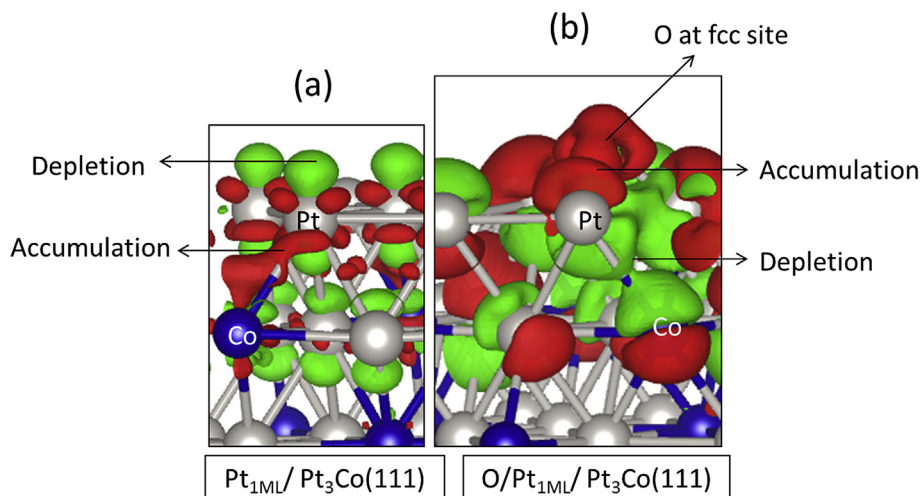


Fig. 9. (a) and (b) show the charge redistribution plot for bare Pt_{1ML}/Pt₃Co(111) system and O-adsorbed Pt_{1ML}/Pt₃Co(111), respectively. Darker regions (red online) indicate accumulation of charge and lighter regions (green online) show depletion of charges. The site of the oxygen adsorption is shown. (For interpretation of the references to color in this figure legend, the reader is referred to the web version of this article.)

coverage. In the case of Pt_{1ML}/Pt₃Co(100), as depicted in Fig. 10, although the same charge redistribution as that of Pt_{1ML}/Pt₃Co(111) can be observed (i.e. accumulation in Pt–O and depletion in Pt–Co region), the bridge site adsorption of oxygen allows for a depletion of charge only along two Pt–Co bonds, leaving the charge distribution in the other Pt–Co bonds unchanged. The fcc site adsorption of O atom in the Pt_{1ML}/Pt₃Co(111), on the other hand, affects all the Pt–Co bonds. This contribute to the positive ΔE for Co migration in (100) facet, and a negative ΔE for (111) facet. It has to be noted, however, that while at (100), the Co migration is endothermic, the magnitude of the ΔE is minimal. Finally, we further note that by virtue of the charge difference expressions above, the Pt–Co bonds deeper into the bulk where the charge densities rarely change, do not show charge density accumulation (or depletion) due to canceling out of same charge densities.

3.4. Effect of Pt-skin composition

In the quest for further lowering Pt loading, a possible substitute metal for the thicker Pt-skin/Pt₃Co systems is investigated. In Fig. 11(a), we show the new Pt_{2ML}/Pt₃Co(111) system with MBL-

substituted Pt mid-layer. The system is denoted now as Pt_{1ML}/MBL/Pt₃Co(111), where MBL = Ru, Rh, Pd, Os, Ir. The (111) surface is used due to the stable hexagonal structure of MBLs. The insertion of the MBL leads to a more stable Pt_{1ML}/MBL/Pt₃Co(111) than the segregated MBL-counterpart: MBL/Pt_{1ML}/Pt₃Co(111). This is evidenced by the lower total energy of the former system (E_A) as shown in Table 3 and furthermore by the relative stability as obtained by the following expression:

$$\Delta E_S = E_A - E_B$$

Here, the E_B is the total energy of the segregated counterpart, MBL/Pt_{1ML}/Pt₃Co(111). The same scheme for Co migration to surface as in Pt_{2ML}/Pt₃Co(111) is used. The ΔE plots under 0.25 ML oxygen coverage are shown in Fig. 11(b). The five Pt_{1ML}/MBL/Pt₃Co(111) systems are compared with that of Pt_{2ML}/Pt₃Co(111). In general, the migration of Co in the Pt mid-layer is endothermic for all systems. Next, the migration from the Pt mid-layer to the surface is exothermic (referenced to the previous step), showing the same Co migration behavior as in the Pt_{2ML}/Pt₃Co(111). With respect to zero energy reference, however, certain MBL-substituted Pt-skin systems exhibit higher positive migration energies than the Pt_{2ML}/

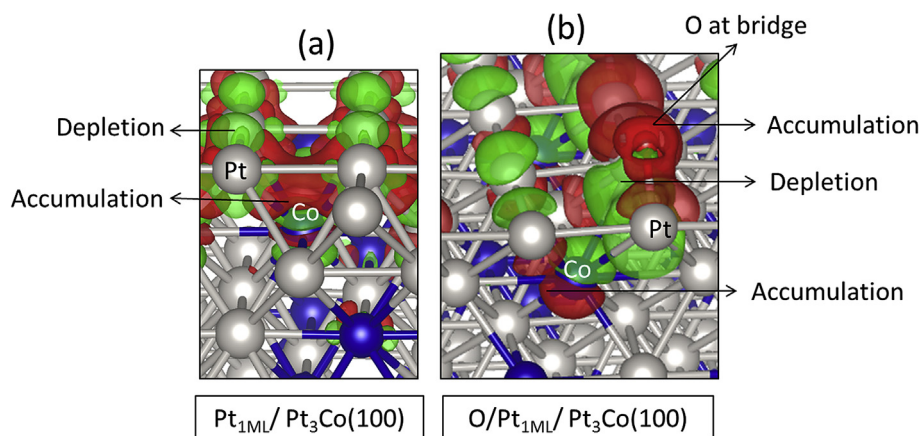


Fig. 10. (a) and (b) show the charge redistribution plot for bare Pt_{1ML}/Pt₃Co(100) system and O-adsorbed Pt_{1ML}/Pt₃Co(100), respectively. Darker regions (red online) indicate accumulation of charge and lighter regions (green online) show depletion of charges. The site of the oxygen adsorption is shown. (For interpretation of the references to color in this figure legend, the reader is referred to the web version of this article.)

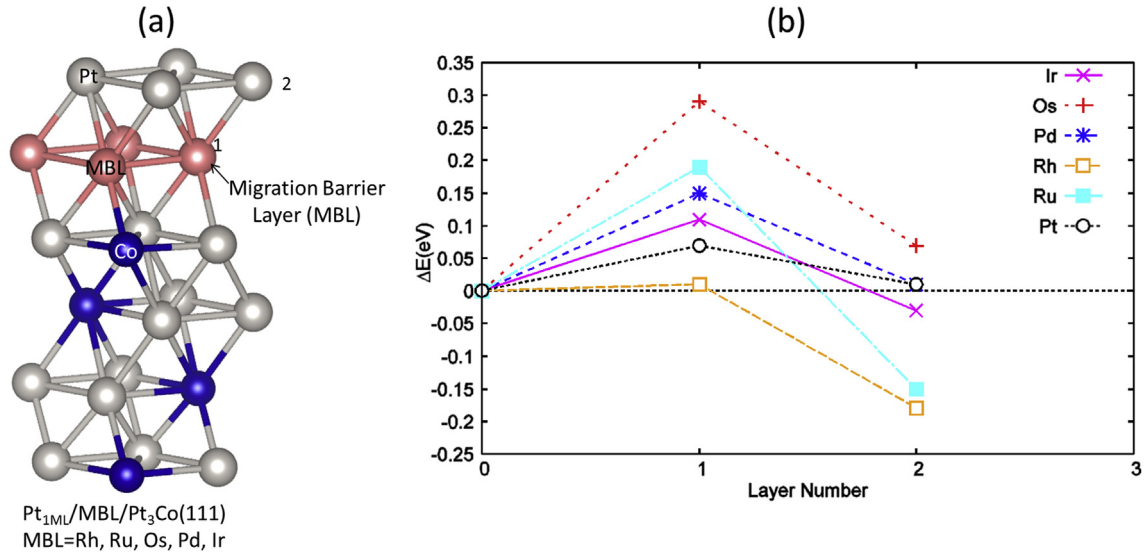


Fig. 11. (a) Migration Barrier Layer (MBL)-substituted Pt-skin system: $\text{Pt}_{1\text{ML}}/\text{MBL}/\text{Pt}_3\text{Co}(111)$, where $\text{MBL} = \text{Ru}, \text{Rh}, \text{Pd}, \text{Os}, \text{Ir}$ and (b) Co migration energy (ΔE plots for $\text{Pt}_{1\text{ML}}/\text{MBL}/\text{Pt}_3\text{Co}(111)$ and $\text{Pt}_{2\text{ML}}/\text{Pt}_3\text{Co}(111)$ under 0.25 ML oxygen coverage.

$\text{Pt}_3\text{Co}(111)$. These are when the MBLs are made of Os and Pd while those that exhibits negative change in migration energies are composed of $\text{MBL} = \text{Ru}, \text{Rh}, \text{Ir}$. Among these, Ir renders the least negative change in energy. Overall, based on the stability against Co migration to surface, the $\text{Pt}_{1\text{ML}}/\text{Os}/\text{Pt}_3\text{Co}(111)$ poses as the most stable system. Furthermore, as pointed out previously, the binding energy of O atom can serve as good predictor of ORR activity in the Pt-skin systems [45,46]. Hence, the binding energies of the O atom in these systems are also calculated and are shown in Table 3. It can be very well noted that the O adsorption are less stable in all the MBL-substituted Pt-skin as compared to that of $\text{Pt}_{2\text{ML}}/\text{Pt}_3\text{Co}(111)$ system. Therefore, $\text{Pt}_{1\text{ML}}/\text{MBL}/\text{Pt}_3\text{Co}(111)$ where $\text{MBL} = \text{Os}, \text{Pd}$ render a more stable and potentially more reactive Pt-skin ORR catalysts.

3.5. Stability against Pt dissolution

Apart from the Co migration to the surface with Co–O bond formation, the dissolution of Pt in both the thicker Pt-skins and the MBL-substituted Pt-skin systems is tested. In the kinetic model of Pt dissolution in PEMFC [47,48], three possible reactions have been well-accepted:

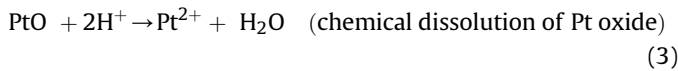
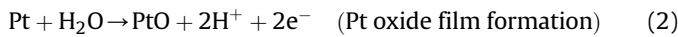
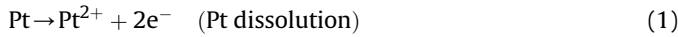
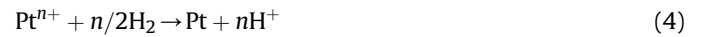


Table 3

Stability data for $\text{Pt}_{1\text{ML}}/\text{MBL}/\text{Pt}_3\text{Co}(111)$ systems with respect to $\text{MBL}/\text{Pt}_{1\text{ML}}/\text{Pt}_3\text{Co}(111)$ systems. E_A is the total energy of the former and E_B is the total energy of the latter. ΔE (eV) is $E_A - E_B$.

A	E_A	B	E_B	ΔE (eV)
$\text{Pt}_{1\text{ML}}/\text{Ir}/\text{Pt}_3\text{Co}(111)$	−154.76	$\text{Ir}/\text{Pt}_{1\text{ML}}/\text{Pt}_3\text{Co}(111)$	−153.04	−1.72
$\text{Pt}_{1\text{ML}}/\text{Os}/\text{Pt}_3\text{Co}(111)$	−163.66	$\text{Os}/\text{Pt}_{1\text{ML}}/\text{Pt}_3\text{Co}(111)$	−161.03	−2.63
$\text{Pt}_{1\text{ML}}/\text{Pd}/\text{Pt}_3\text{Co}(111)$	−141.12	$\text{Pd}/\text{Pt}_{1\text{ML}}/\text{Pt}_3\text{Co}(111)$	−140.91	−0.20
$\text{Pt}_{1\text{ML}}/\text{Rh}/\text{Pt}_3\text{Co}(111)$	−149.24	$\text{Rh}/\text{Pt}_{1\text{ML}}/\text{Pt}_3\text{Co}(111)$	−147.63	−1.61
$\text{Pt}_{1\text{ML}}/\text{Ru}/\text{Pt}_3\text{Co}(111)$	−156.39	$\text{Ru}/\text{Pt}_{1\text{ML}}/\text{Pt}_3\text{Co}(111)$	−153.82	−2.57

Therefore, there are two ways by which Pt is lost to the solution, the first is the electrochemical dissolution of Pt according to reaction (1) and the second is the chemical dissolution of PtO film according to reaction (3). The fact that (3) is regarded as a slow reaction and that it occurs at high potentials (when the Pt surface is covered with an oxide film), the viability of reaction (1) as basis for evaluation of Pt dissolution at zero and low oxygen coverage (0.25 ML) is clear. When the dissolution of Pt is referenced to the standard hydrogen electrode (SHE), then the redox reaction (1) {with full description of net reaction for the reference and working electrode system} can be rewritten as:



and the Gibbs free energy change of the reaction is:

$$\Delta G = \mu_{\text{Pt}} + \mu_{n\text{H}^+} - \mu_{\text{Pt}^{n+}} - \mu_{n/2\text{H}_2} \quad (5)$$

where μ_{Pt} , $\mu_{\text{Pt}^{n+}}$ are the chemical potentials of pure metal Pt and Pt ions (and that equilibrium exists between Pt in the system and the dissolved Pt in the solution) and $\mu_{n\text{H}^+}$, $\mu_{n/2\text{H}_2}$ are the chemical potentials of H^+ and H_2 (at standard conditions). The ΔG is related to the electrochemical potential by:

$$\Delta G = neU_{\text{Pt}} = \mu_{\text{Pt}} + \mu_{n\text{H}^+} - \mu_{\text{Pt}^{n+}} - \mu_{n/2\text{H}_2} \quad (6)$$

For other type of Pt systems, denoted as Pt' , equation (6) is thus:

$$neU_{\text{Pt}'} = \mu_{\text{Pt}'} + \mu_{n\text{H}^+} - \mu_{\text{Pt}'^{n+}} - \mu_{n/2\text{H}_2} \quad (7)$$

and the shift in the electrode potential is (after cancellation of same terms):

$$ne(U_{\text{Pt}'} - U_{\text{Pt}}) = \mu_{\text{Pt}'} - \mu_{\text{Pt}} \quad (8)$$

In this work, the chemical potentials are calculated based on Pt vacancy formation energy, E_{des} , in the presence of 0.25 ML oxygen coverage:

$$E_{\text{des}} = (E_{\text{Pt}} + E_{\text{O}/\text{Pt}_{\text{vac}}}) - E_{\text{O}/\text{Pt}} \quad (9)$$

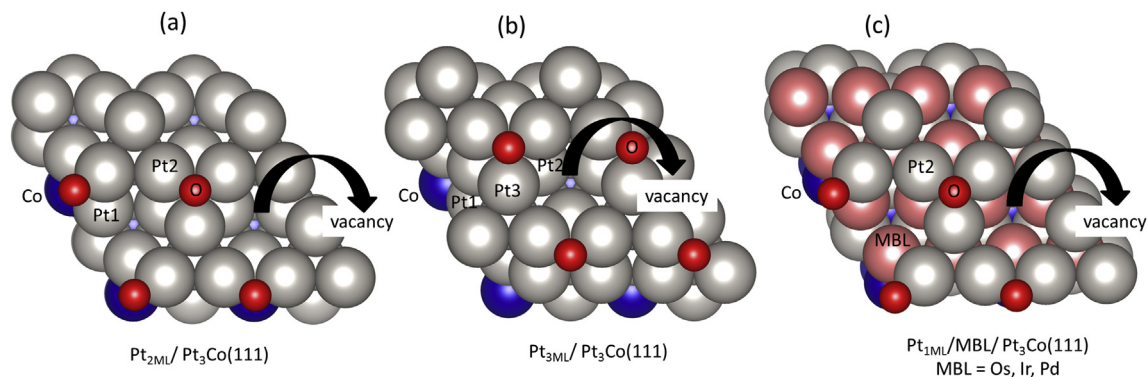


Fig. 12. (a), (b) and (c) show the atomic structure of $\text{Pt}_{2\text{ML}}/\text{Pt}_3\text{Co}(111)$, $\text{Pt}_{3\text{ML}}/\text{Pt}_3\text{Co}(111)$ and $\text{Pt}_{1\text{ML}}/\text{M}/\text{Pt}_3\text{Co}(111)$ with 1 Pt atom vacancy, respectively. The Pt, Co and O atoms are shown.

where E_{Pt} , $E_{\text{O/Pt}_{\text{vac}}}$ and $E_{\text{O/Pt}}$ are the total energies of isolated Pt atom, O/Pt with 1 Pt vacancy and the O/Pt slab systems, respectively. Fig. 12(a)–(c) shows the optimized $\text{Pt}_{2-3\text{ML}}/\text{Pt}_3\text{Co}(111)$ and $\text{Pt}_{1\text{ML}}/\text{MBL}/\text{Pt}_3\text{Co}(111)$ systems with 1 Pt atom vacancy. Similarly for other types of Pt systems, Pt:

$$E'_{\text{des}} = (E_{\text{Pt}} + E_{\text{O/Pt}_{\text{vac}}}) - E_{\text{O/Pt}} \quad (10)$$

Thus, finally:

$$\mu_{\text{Pt}} - \mu_{\text{Pt}} = E'_{\text{des}} - E_{\text{des}} = (E_{\text{O/Pt}_{\text{vac}}} - E_{\text{O/Pt}}) - (E_{\text{O/Pt}_{\text{vac}}} - E_{\text{O/Pt}}) \quad (11)$$

$$\Delta U = U_{\text{Pt}} - U_{\text{Pt}} = (\mu_{\text{Pt}} - \mu_{\text{Pt}})/ne \quad (12)$$

Table 4 shows the chemical potential and electrode potential shifts for several Pt systems. The reference system is Pt(111). The thicker Pt-skin systems $\{\text{Pt}_{2-3\text{ML}}/\text{Pt}_3\text{Co}(111)\}$ have a very minimal negative shift in the electrode potential (i.e. -0.09 V and -0.06 V). Thus, it can be considered that their stability against Pt dissolution should almost be the same as that of pure Pt(111). For the $\text{Pt}_{1\text{ML}}/\text{MBL}/\text{Pt}_3\text{Co}(111)$ systems, where MBL = Os, Pd and Ir, Pt dissolution occurs at higher potentials as compared to that of $\text{Pt}_{2-3\text{ML}}/\text{Pt}_3\text{Co}(111)$. Interestingly, those composed of Os and Pd are in fact exhibiting a *positive potential shift*. This suggests better stability than the pure Pt(111) itself. The $\text{Pt}_{1\text{ML}}/\text{Os}/\text{Pt}_3\text{Co}(111)$ is the most stable against Pt dissolution with a high positive potential shift of 0.16 V. Since Os is four to five times cheaper than Pt, then this MBL offers a potential low-cost Pt-skin composition for a Pt-skin-based ORR catalyst.

4. Summary

First-principles study based on DFT is conducted to evaluate the stability of Pt-skin/ Pt_3Co systems against Co migration and Pt dissolution as a function of Pt-skin thickness, surface structure and

Table 4
Adsorption energies of O atom on the Pt systems; and the chemical potential and electrochemical potential shift for Pt systems.

Pt Systems	E_{ads}	$\mu_{\text{Pt}} - \mu_{\text{Pt}}$	ΔU
$\text{Pt}_{2\text{ML}}/\text{Pt}_3\text{Co}(111)$	−4.30	−0.18	−0.09
$\text{Pt}_{3\text{ML}}/\text{Pt}_3\text{Co}(111)$	−4.32	−0.11	−0.06
$\text{Pt}_{1\text{ML}}/\text{Os}/\text{Pt}_3\text{Co}(111)$	−4.20	0.31	0.16
$\text{Pt}_{1\text{ML}}/\text{Pd}/\text{Pt}_3\text{Co}(111)$	−4.27	0.06	0.03
$\text{Pt}_{1\text{ML}}/\text{Ir}/\text{Pt}_3\text{Co}(111)$	−4.26	−0.08	−0.04

composition. It is found that the thicker Pt-skin ($\text{Pt}_{2-3\text{ML}}/\text{Pt}_3\text{Co}$) in both the (100) and (111) facets under 0.25 ML oxygen coverage are more stable than $\text{Pt}_{1\text{ML}}/\text{Pt}_3\text{Co}$ counterpart, confirming the observed stability in thicker Pt-skin systems on Pt–Co alloys in experiments. The enhanced stability is attributed to the positive change in energy (ΔE for Co migration within the Pt mid-layers as well as the no found effect of adsorbed O atom on the Co movement within the Pt-skin. However, it has to be noted that the behavior of migration of Co from the subsurface to the Pt-skin surface is different for different facets. We note that the Co migration is exothermic in (111) and endothermic in (100) surface structures. Charge difference plots reveal that upon oxygen adsorption, the charge depletion in Pt–Co bond is less in (100) facet compared to that of (111). This is due to the bridge site adsorption of oxygen in $\text{Pt}_{1\text{ML}}/\text{Pt}_3\text{Co}(100)$ as compared to the hollow site (fcc) adsorption in $\text{Pt}_{1\text{ML}}/\text{Pt}_3\text{Co}(111)$. Furthermore, the stability against Pt dissolution in the thicker Pt-skin system, $\text{Pt}_{2-3\text{ML}}/\text{Pt}_3\text{Co}(111)$, is evaluated. It is noted that a very minimal negative electrochemical potential shift is exhibited by the Pt-skin systems, signifying a stability close to the reference system, Pt(111). Lastly, the Pt-skin composition is varied by substituting Migration Barrier Layer (MBL) for the Pt mid-layer in the thicker Pt-skin [i.e. $\text{Pt}_{1\text{ML}}/\text{MBL}/\text{Pt}_3\text{Co}(111)$]. The MBL is a 4d or a 5d transition metal: Ru, Rh, Ir, Os, Pd. The stability against Co migration and Pt dissolution under oxygen coverage is also tested. It is observed that on all the $\text{Pt}_{1\text{ML}}/\text{MBL}/\text{Pt}_3\text{Co}(111)$ systems, the oxygen binding energy is less than on the corresponding $\text{Pt}_{2\text{ML}}/\text{Pt}_3\text{Co}(111)$ as well as on the Pt(111). The Co migration to surface in $\text{Pt}_{1\text{ML}}/\text{MBL}/\text{Pt}_3\text{Co}(111)$, where M is Os and Pd is best inhibited as compared to that of the $\text{Pt}_{2\text{ML}}/\text{Pt}_3\text{Co}(111)$ and the other MBL-substituted Pt-skins, due to their higher positive magnitude for ΔE . The electrochemical potential shift for Pt dissolution for the thicker Pt-skins $\{\text{Pt}_{2-3\text{ML}}/\text{Pt}_3\text{Co}(111)\}$ and for MBL-substituted Pt skins $\{\text{Pt}_{1\text{ML}}/\text{MBL}/\text{Pt}_3\text{Co}(111)\}$ shows that the thicker Pt-skins have almost the same Pt stability as that of Pt(111). It is noteworthy that the MBL-substituted Pt-skin systems are in fact more stable than the thicker Pt-skin systems against Pt dissolution. Screening of MBLs based on the electrochemical potential shift for Pt dissolution picks out M = Os and Pd as the best substitution metal due to the positive electrode potential shift. This means that $\text{Pt}_{1\text{ML}}/\text{Os}/\text{Pt}_3\text{Co}(111)$ and $\text{Pt}_{1\text{ML}}/\text{Pd}/\text{Pt}_3\text{Co}(111)$ are more stable than the Pt(111) itself. Strikingly, $\text{Pt}_{1\text{ML}}/\text{Os}/\text{Pt}_3\text{Co}(111)$ gives highest positive potential shift of ~ 0.16 V. Because Os is much cheaper than Pt and that it gives both the highest positive electrode potential shift for Pt dissolution and the largest magnitude for ΔE for Co migration than the rest of the MBLs, then Os poses a highly viable compositional material for a low-cost, stable and active Pt-skin ORR catalyst for PEMFC.

Acknowledgments

M.C.S. Escaño extends gratitude to Tenure Track Program for Innovative Research, Ministry of Education, Culture, Sports, Science and Technology, Japan (MEXT) and Japan Science and Technology Agency (JST) for research funding. Some of the calculations are done using Kyoto University Supercomputer and High-Performance Computing System (HPCS) of Escaño Research Group, University of Fukui.

References

- [1] T. Toda, H. Igarashi, H. Uchida, M. Watanabe, *J. Electrochem. Soc.* 146 (1999) 3750–3756.
- [2] U.A. Paulus, A. Wokaun, G.G. Scherer, T.J. Schmidt, V. Stamenkovic, V. Radmilovic, N.M. Markovic, P.N. Ross, *J. Phys. Chem. B* 106 (2002) 4181–4191.
- [3] V.R. Stamenkovic, B.S. Mun, M. Arenz, K.J.J. Mayrhofer, C.A. Lucas, G. Wang, P.N. Ross, N.M. Markovic, *Nat. Mater.* 6 (2007) 241–247.
- [4] N. Wakabayashi, M. Takeichi, H. Uchida, M. Watanabe, *J. Phys. Chem. B* 109 (2005) 5836–5841.
- [5] E. Antolini, J.R.C. Salgado, E.R. Gonzales, *J. Power Sources* 160 (2006) 957–968.
- [6] B.C. Beard, P.N. Ross, *J. Electrochem. Soc.* 137 (1990) 3368–3373.
- [7] S. Koh, J. Leisch, M.F. Toney, P. Strasser, *J. Phys. Chem. C* 111 (2007) 3744–3752.
- [8] M. Watanabe, D.A. Tryk, M. Wakisaka, H. Yano, H. Uchida, *Electrochim. Acta* 84 (2012) 187–201.
- [9] A. Stassi, I. Gatto, G. Monforte, E. Passalacqua, V. Antonucci, A.S. Arico, *ECS Trans.* 35 (2011) 83–91.
- [10] V.R. Stamenkovic, B.S. Mun, K.J.J. Mayrhofer, P.N. Ross, N.M. Markovic, *J. Am. Chem. Soc.* 128 (2006) 8813–8819.
- [11] L.J. Wan, T. Moriyama, M. Ito, H. Uchida, M. Watanabe, *Chem. Commun.* (2002) 58–59.
- [12] K. Okaya, H. Yano, K. Kakinuma, M. Watanabe, H. Uchida, *Appl. Mater. Interfaces* 4 (2012) 6982–6991.
- [13] D. Wang, H.L. Xin, R. Hovden, H. Wang, Y. Yu, D.A. Muller, F.J. Disalvo, H.D. Abruna, *Nat. Mater.* 12 (2013) 81–87.
- [14] P.B. Balbuena, R. Calleja-Tovar, P. Hirunsit, J.M. Martinez de la Hoz, Y. Ma, G.E. Ramirez-Caballero, *Top. Catal.* 55 (2012) 322–335.
- [15] J. Greeley, J.K. Norskov, *Electrochim. Acta* 52 (2007) 5829–5836.
- [16] C.A. Menning, H.H. Hwu, J.G. Chen, *J. Phys. Chem.* 110 (2006) 15471–15477.
- [17] S.H. Noh, M.H. Seo, J.K. Seo, P. Fischer, B. Han, *Nanoscale* 5 (2013) 8625–8633.
- [18] K. Srinivasan, S.N. Piramanayagam, R. Sbiaa, *Appl. Phys. Lett.* 93 (2008) 072503–072505.
- [19] F. Manders, K.J. Veenstra, A. Kirilyuk, T.H. Rasing, H.A.M. van den Berg, N. Persat, *Appl. Phys. Lett.* 73 (1998) 3601–3603.
- [20] S.Y. Chen, J.M. Wu, Y.D. Yao, H.H. Huang, C.C. Yu, *J. Appl. Phys.* 107 (2010), 09A714–09A717.
- [21] P. Hohenberg, W. Kohn, *Phys. Rev.* 136 (1964) B864–B871.
- [22] W. Kohn, L.J. Sham, *Phys. Rev.* 140 (1965) A1133–A1138.
- [23] G. Kresse, J. Joubert, *Phys. Rev. B* 59 (1999) 1758–1775.
- [24] G. Kresse, J. Furthmüller, *Comput. Mater. Sci.* 6 (1996) 15–50.
- [25] G. Kresse, J. Furthmüller, *Phys. Rev. B* 54 (1996) 1169–1186.
- [26] G. Kresse, J. Hafner, *Phys. Rev. B* 47 (1993) 558–561.
- [27] G. Kresse, J. Hafner, *Phys. Rev. B* 49 (1994) 14251–14269.
- [28] M.P. Teter, M.C. Payne, D.C. Allan, *Phys. Rev. B* 40 (1989) 12255–12263.
- [29] J.P. Perdew, K. Burke, M. Ernzerhof, *Phys. Rev. Lett.* 77 (1996) 3865–3868.
- [30] M. Methfessel, A. Paxton, *Phys. Rev. B* 40 (1989) 3616–3621.
- [31] C. Kittel, *Introduction to Solid State Physics*, Wiley, New York, 1996.
- [32] G.R. Haro, R.F.C. Farrow, D. Weller, T.A. Rabedeau, R.F. Marks, *Phys. Rev. B* 48 (1993) 17538–17544.
- [33] A. Kootte, C. Haas, R.A. De Groot, *J. Phys. Condens. Matter* 3 (1991) 1133–1152.
- [34] *CRC Handbook of Chemistry and Physics*, 86th ed., CRC Press, Boca Raton, FL, 2005.
- [35] Q. Ge, P. Hu, D.A. King, M.-H. Lee, J.A. White, M.C. Payne, *J. Chem. Phys.* 106 (1997) 1210–1215.
- [36] Y. Xu, M. Mavrikakis, *J. Chem. Phys.* 166 (2002) 10846–10854.
- [37] A.V. Ruban, H.L. Skriver, J.K. Norskov, *Phys. Rev. B* 59 (1999) 15990–16000.
- [38] M.C. Escaño, T.Q. Nguyen, H. Nakanishi, H. Kasai, *J. Phys. Condens. Matter* 21 (2009) 492201–492206.
- [39] M.C. Escaño, T.Q. Nguyen, H. Nakanishi, H. Kasai, *Surf. Sci.* 602 (2008) 3415–3423.
- [40] M.P. Hyman, J. Will Medlin, *J. Phys. Chem. C* 111 (2007) 17052–17060.
- [41] J.R. Kitchin, J.K. Norskov, M.A. Barteau, J.G. Chen, *J. Chem. Phys.* 120 (2004) 10240–10246.
- [42] D.M. Wood, A. Zunger, *J. Phys. A* 18 (1985) 1343.
- [43] P. Pulay, *Chem. Phys. Lett.* 73 (1980) 393–398.
- [44] A. Eichler, F. Mittendorfer, J. Hafner, *Phys. Rev. B* 62 (2000) 4744–4754.
- [45] A.U. Nilekar, M. Mavrikakis, *Surf. Sci. Lett.* 602 (2008) L89–L94.
- [46] V. Stamenkovic, B.S. Mun, K.J.J. Mayrhofer, P.N. Ross, N.M. Markovic, J. Rossmeisl, J. Greeley, J. Norskov, *Angew. Chem. Int. Ed.* 45 (2006) 2897–2901.
- [47] R.M. Darling, J.P. Meyers, *J. Electrochem. Soc.* 150 (2003) A1523–A1527.
- [48] A. Wachter, K.P. Bohnen, K.M. Ho, *Ann. Phys.* 6 (1996) 215–223.